20

In-Situ Mechanical Testing of Nano-Component in TEM

Takashi Sumigawa and Takayuki Kitamura
Department of Mechanical Engineering and Science, Kyoto University, Japan

1. Introduction

MEMS (Micro electro mechanical system) and NEMS (Nano electro mechanical system), which are composed of large number of submicron- or nano-scale dissimilar components, often experience extrinsic loads due to operational and environmental conditions and these bring about local fracture. In order to make an accurate life prediction, the mechanical properties of components (e.g., deformation, fracture, and fatigue behaviour) have to be understood well. Especially, there are numerous uncertainties reported in the mechanical properties of micro-nano scale components, which are different from those of macroscopic one.

1. Smaller metals than a micrometer possess different plastic deformation properties from those of the bulk (Vinci et al., 1995; Xiang et al., 2006) because small volume components require a large driving force for dislocation generation and glide due to the dislocation source starvation (Greer & Nix, 2006; Hou et al., 2008; Liu et al., 2009) and the mirror force from free surfaces (J. Weertman & J.R Weertman, 1964). Furthermore, since the components in device are usually surrounded by dissimilar materials, the resulting deformation constraint affects the plastic behaviour as well.
2. Dissimilar interface is one of the most favorable potential crack initiation sites in a micro- and nano-scale component because it often has weak bonding (low resistance to fracture) and stress concentration (high driving force to fracture) due to the deformation mismatch between dissimilar materials (Bogy, 1968). In the component, the region governed by the stress concentration is confined in the nano-scale. In such case, the applicability of continuum mechanics to the crack initiation is questionable.
3. It is well known that irreversible cyclic deformation results in characteristic dislocation structures (vein, ladder-structure, and cell) in fatigue of bulk metals (Mughrabi, 1978; Thompson et al., 1956; Winter, 1978). In particular, the ladder and cell structures cause crack initiation owing to the strain localization because they are much softer than the matrix (Suresh, 1998). These fatigue substructures have a size in the scale of a few micrometers (Mughrabi, 1978). However, since the strain-concentrated region in nano-components is a few nanometers or at most a few tens of nanometers, typical fatigue substructure cannot form there.

Although we have to specify the mechanical properties of nano-component, the strength evaluation experiment of nano-component involves some major challenges in I.

Observation, II. Experimental set-up, III. Specimen fabrication, and IV. Specimen gripping and alignment. Consequently, we have to use special devices and methods described below for the investigation.

I. Observation

For observation of nano-components, electron microscopes (e.g., transmission electron microscope (TEM) and scanning electron microscope (SEM)) are required because nano-components are invisible at optical wavelength. TEM is better in terms of image resolution while SEM possesses the depth of focus in the surface observation.

II. Experimental set-up

Piezoelectric device (Keller et al., 1996; Liu et al., 2009; Tsuchiya et al., 2000) and electromagnetic actuator (Kim & Huh, 2011; Komai et al., 1998), which can control nanometer order displacement, are used as an actuator. Load is measured by means of capacitive load cell (Zhu et al., 2005). Laser displacement meter (Burdess et al., 1997; Yi et al., 2000) and image analysis (Cheng et al., 2005; Hua et al., 2007) can detect specimen displacement with nanometer-scale resolution.

III. Specimen fabrication

Specimen is usually fabricated by means of wet-etching (Li et al., 2005; Namazu et al., 2002), dry-etching (Ryu et al., 2006 ; Tripathy et al., 2007), and focused ion beam (FIB) processing (Dimiduk et al., 2005; Motz et al., 2005). Wet-etching is often applied to single crystal Si, which is an important material in MEMS devices. Dry-etching and FIB processing are used for processing of multi-layered and composite materials.

IV. Specimen gripping and alignment

Although tensile testing is popular for evaluation of mechanical properties, it is difficult to apply it to nano-component because it requires precise alignment and reliable gripping (Haque & Saif, 2002; Huang & Spaepen, 2000; Tsuchiya et al., 1998). Especially, bending (Motz et al., 2005; Namazu et al., 2000) and compression (Dimiduk et al., 2005 ; Moser & Wasmer, 2007) methods are often adopted. Bending one has an advantage in terms of examination on the fracture behaviour.

In this chapter, we introduce bending experiment of nano-component in a TEM for *in-situ* observation. The material is composed of silicon (Si), copper (Cu), and silicon nitride (SiN), and the focus is on the deformation of nano-metal (Cu) and the fracture along the Si/Cu interface.

2. Mechanical testing with *in-situ* TEM observation (Sumigawa et al., 2010a, 2010b, 2010c, 2011a, 2011b)

Figure 1 schematically illustrates specimen configuration and loading scheme. The tested parts of Si, Cu, and SiN are in 100 nm order, and Si/Cu and Cu/SiN interfaces are vertically arranged in the cantilever. Load is applied to the SiN layer away from the Cu portion by means of a diamond tip. The residual stress in each layer is examined beforehand (See Table

1), and the influence is included in the finite element method (FEM) stress analysis in the following sections.

	Residual stress [MPa]
20 nm-thick Cu film (Sumigawa et al., 2010a)	760 MPa
200 nm-thick Cu film	150 MPa
500 nm-thick SiN layer (Sumigawa et al., 2010a)	-290 MPa

Table 1. Residual stresses of 20 nm-thick, 200 nm-thick Cu films and SiN layer.

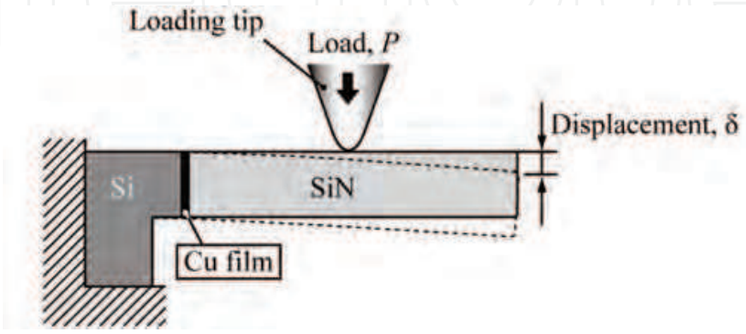

Fig. 1. Schematic illustration of bending experiment.

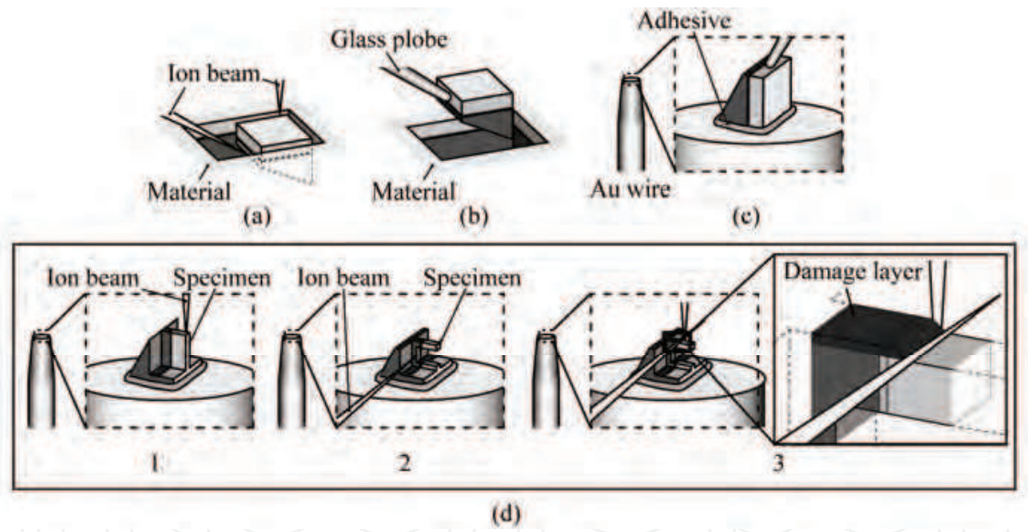

Fig. 2. Specimen fabrication procedure.

The specimen is carved out by means of focused ion beam (FIB) processing from a multilayer material, where Cu and SiN are deposited on a Si substrate by magnetron sputtering. The fabrication procedure of specimen is as follows.

1. A block with a size of about 10×10×10 μm^3 is carved out from the multilayer material. (Fig. 2(a))
2. The block is picked up by a micro glass probe using electrostatic force. (Fig. 2(b))
3. A gold (Au) wire with a flat top is prepared, and the block is mounted using an adhesive. (Fig. 2(c))

4. The block is formed into a cantilever-shaped specimen. (Fig. 2(d) from 1 to 3)
   1. The side planes are processed by a vertical FIB. (Fig. 2(d)-1)
   2. The top and the bottom planes of the cantilever are processed by a lateral FIB. (Fig. 2(d)-2)
   3. The surfaces are finished to remove the layer damaged by the crude processing, and the shape of the interface edge is flattened (Fig. 2(d)-3)

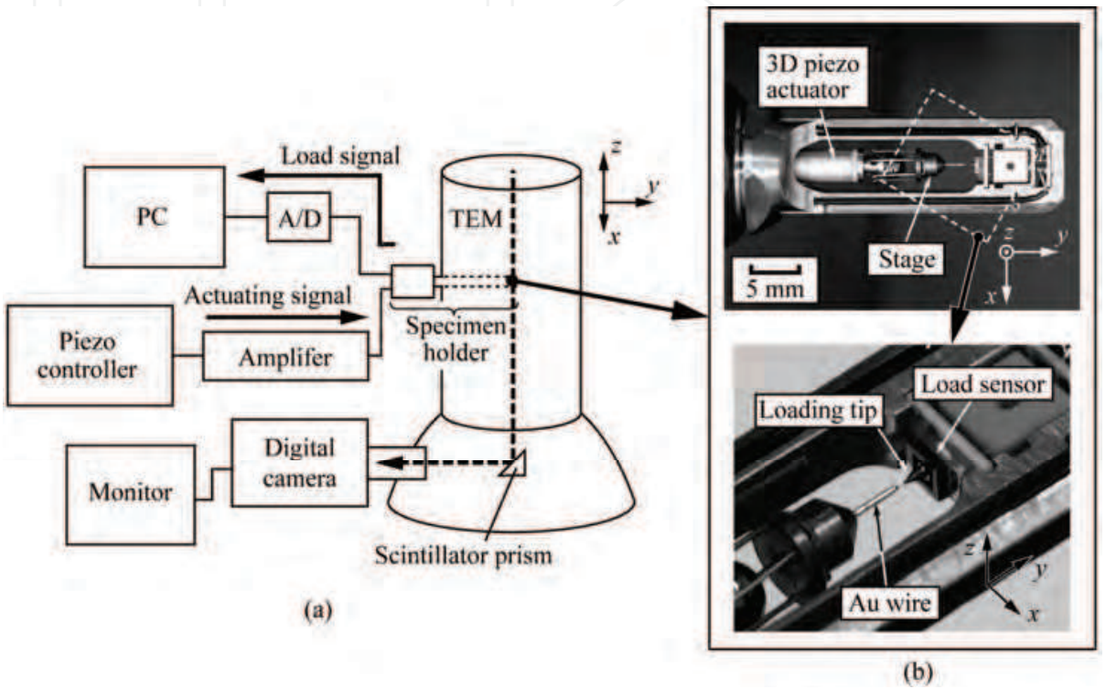

Fig. 3. (a) System of loading experiment with *in-situ* TEM observation, and (b) detail of loading apparatus.

The output voltage of the FIB processing is kept at 30 kV, and the currents in the crude processing and in the surface finishing are 5-10 nA and 10 pA, respectively.

Figure 3(a) shows a schematic illustration of experimental set-up. It consists of a TEM (JEOL, JEM-2100), a specimen holder with a mechanical loading apparatus (Nanofactory Instruments AB, SA2000N), a piezo controller, and a digital camcorder. Figure 3(b) shows the loading apparatus, which consists of a stage which can move in three orthogonal directions and a conical diamond tip with a capacitance load sensor. The measurement range and accuracy of the load are 0-100 μN and ±0.1 μN, respectively.

An Au wire, which holds the specimen, is connected to the stage, and a load is applied by pressing the specimen onto the diamond tip. The applied load, P, is directly detected by means of the load sensor attached to the back of the tip. The displacement at the specimen end, δ, (See Fig. 1) is measured using a TEM with the loading device installed. TEM observation has the advantages of precise measurement of displacement and precise identification of exact locations of the interfaces and contact area of the loading tip. The observations are carried out with an accelerating voltage of 200 kV under a vacuum of 1.5×10^{-5} Pa.

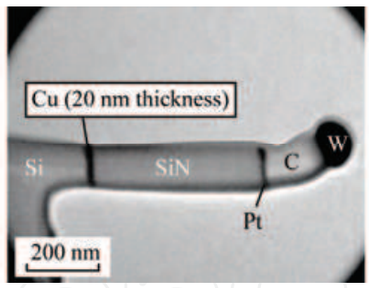

Fig. 4. Bright-field TEM image of cantilever specimen.

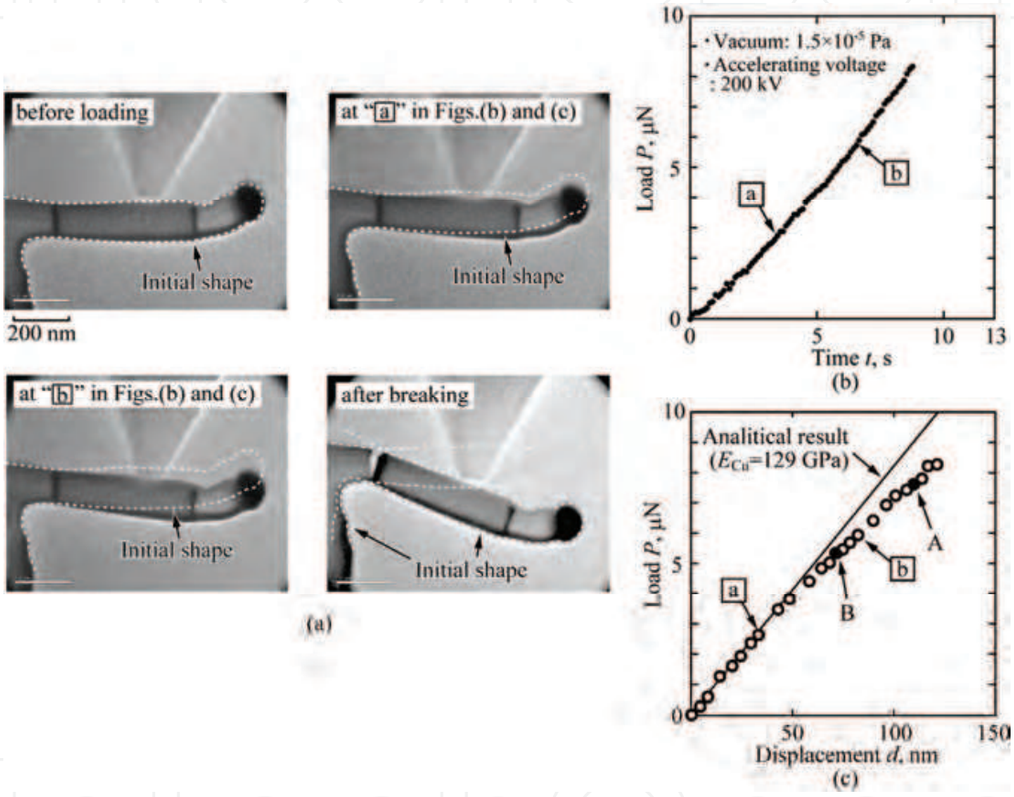

Fig. 5. Deformation behaviour of cantilever specimen: (a) bright-field TEM images, (b) load-time curve, and (c) load-displacement curve.

3. Mechanical properties of nano-component

3.1 Plasticity in 20 nm-thickness Cu film (Sumigawa et al., 2010a)

3.1.1 Research target and experimental detail

Although some researchers have clarified the plastic property of micron-thickness thin film by means of the indentation method (Dao et al., 2001; Huang et al., 2000), it is extremely difficult to apply the method to nano-components because measurement error becomes large owing to the identification of exact tip shape and sample roughness. Thus, the target in this section is to investigate the plastic behaviour of nano-metal by using the bending experiment under the *in-situ* TEM observation.

Figure 4 shows the bright-field TEM image of specimen. The cantilever arm is extended in order to magnify the deformation in Cu. The difference in transmission rates of the dissimilar materials enables us to recognize the location of dissimilar interfaces in the TEM micrograph. The target material to specify the plasticity is Cu with the dimension of 280 nm × 125 nm × 20 nm, which is sandwiched by Si and SiN.

3.1.2 Inverse analysis

Figure 5 shows (a) bright-field TEM images before and during loading, (b) the relationship between the applied load, P, and the time, t, (P-t relationship), and (c) the relationship between P and the displacement at the cantilever tip (arm end of specimen), δ, (P-δ relationship). The loading point and the Cu film are clearly identified by the TEM, and the displacement at the arm end can be quantitatively measured from the images. The P-t relationship (Fig. 5(b)) indicates smooth loading during the experiment. In Fig. 5(c), the displacement increases linearly with increasing load at low loading levels. The solid line in Fig. 5(c) shows the relation obtained by elastic FEM simulation, where all materials are assumed to be linear-elastic and the Young's modulus of the bulk material (E_{Cu} = 129 GPa) is used for the Cu film. The good agreement with the experimental results at low loading levels indicates that the structure of the film has little effect on the Young's modulus. The P-δ relationship shows clear nonlinear behaviour beyond P = 3 μN, where the deviation greatly exceeds the measurement smallest limit (about 5 nm). Since the TEM image after the breaking points out that the Si and the SiN parts keep the original shape and size, they elastically deform during the loading. In short, the nonlinearity in the P-δ relationship is due to the plasticity of Cu film.

The Cu portion is too thin to measure the deformation quantitatively by the TEM image. Thus, the elasto-plastic constitutive equation of the Cu film is derived by inverse analysis using the P-δ relation and a three-dimensional FEM.

Using the Von Mises equivalent stress and strain, the deformation behaviour of the Cu film is described by

$$\sigma = \begin{cases} E\varepsilon & , for\ \sigma \le \sigma_y \\ R\varepsilon^n & , for\ \sigma \ge \sigma_y \end{cases}, \tag{1}$$

where E, R, n, ε, and σ_y are the Young's modulus, strength coefficient, strain hardening exponent, total effective strain, and yield stress, respectively. At the yield point, as we have

$$\frac{\sigma_y}{R} = \left(\frac{\sigma_y}{E} \right)^n \tag{2}$$

R is given by the quantities E, σ_y, and n. Since we can use the bulk elastic constants as shown in Fig. 5(c), the unknown parameters are only σ_y and n.

The derivation procedure of σ_y and n is as follows:

1. Arbitrary points (points A and B) are picked up in the non-linear portion of the load-displacement curve (Fig. 6(a)).
2. The combination of σ_y and n, which fulfills the displacement at the point A as measured by the experiment, is found using elasto-plastic FEM by trial-and-error (Fig. 6(b)). Since two parameters cannot be determined at once from one experimental point, all sets of (σ_y, n), which satisfy the non-linear deformation at the point A, have a relationship schematically shown in Fig. 6(b)
3. By the same way, the combination of σ_y and n at point B is derived through FEM (Fig. 6(c)). The broken line in Fig. 6(c) shows the relationship determined from point B.
4. The intersection between the two lines gives the adequate combination of σ_y and n (Fig. 6(c)) for the constitutive equation of nano-Cu.

The points A (109.5 nm, 7.6 μN) and B (71.0 nm, 5.3 μN) in the *P*-*d* relationship are picked up for the inverse analysis.

For the accurate analysis, it is important to identify the exact shape of the specimen. The FEM model is prepared using commercial three-dimensional CAD (computer aided design) software. The model is divided into meshes as shown in Fig. 7, where the region near the interface has finer mesh. A perfect constraint condition is imposed on the left and bottom edges of the model, and the elastic constants in the analysis are summarized in Fig. 7.

Figure 8(a) shows the σ_y-n relationships at points A and B (Fig. 5(c)) obtained by the inverse analysis. The intersection gives the following elasto-plastic constitutive equation for the 20 nm-thick Cu film:

$$\sigma = \begin{cases} 129000\varepsilon & \text{, for } \sigma \le 765 \quad [MPa] \\ 3316\varepsilon^{0.3} & \text{, for } \sigma \ge 765 \quad [MPa] \end{cases}. \tag{3}$$

Figure 8(b) shows the *P*-δ relationship (solid line) obtained by the FEM on the basis of Eq. (3). This demonstrates that Eq. (3) consistently reproduces the nonlinearity of the Cu film.

Figure 9 shows the tensile behaviour obtained and those of a 200 nm-thick Cu film (Hirakata et al., 2007) and a Cu bulk material (average diameter of grains is 58 μm) (ASM Handbook, 2000) for comparison. The yield stress of the bulk material is the lowest (σ_y = 60 MPa), and increases with decreasing thickness of the film (200 nm-thick: σ_y = 272 MPa, 20 nm-thick: σ_y = 765 MPa).

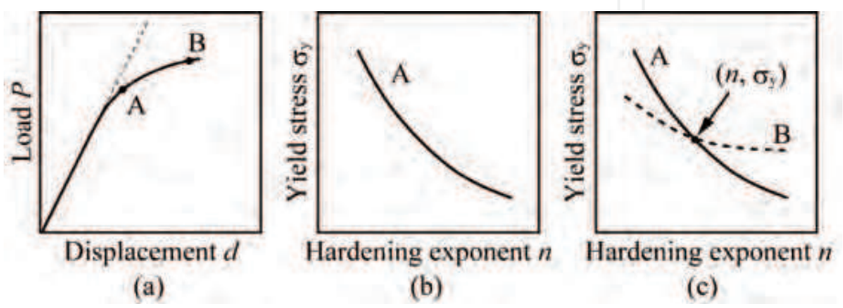

Fig. 6. Procedure for inverse analysis.

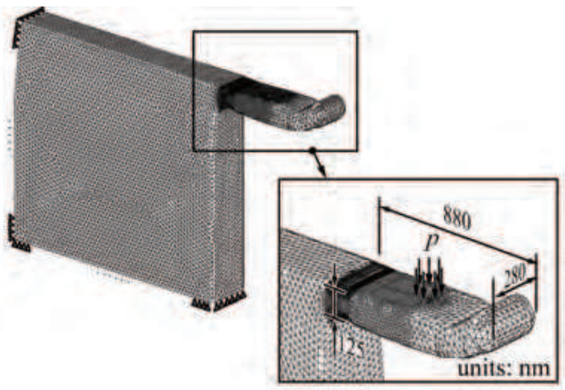

Material	E (GPa)	ν
SiN	197	0.27
Pt	168	0.377
C	10	0.3
W	407	0.17

Material	C_{11}(GPa)	C_{12}(GPa)	C_{44}(GPa)
Si	167.4	65.23	79.57

Fig. 7. Analytical model and material constants in FEM analysis.

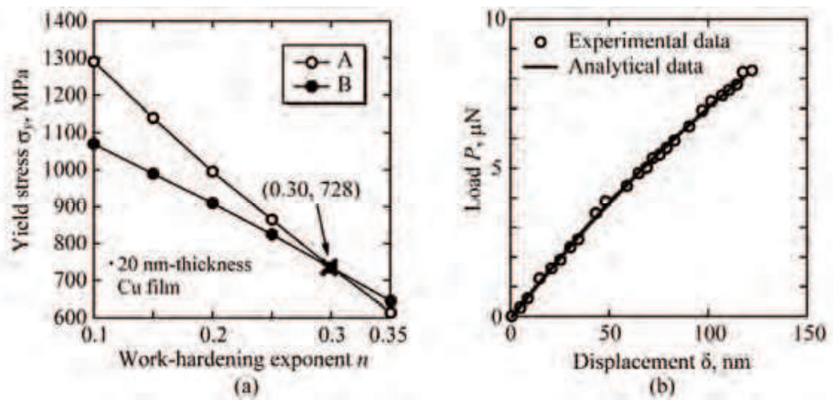

Fig. 8. (a) σ_y-n relationships of points A and B, and (b) loading curves obtained from the inverse analysis.

If the mean grain diameter is assumed to be film thickness, the Hall-Petch relation of spattered Cu films (20 nm thickness) (Ruud et al., 1993) gives the yield stress of about 1 GPa. Similarly, it gives about 250 MPa for the grain diameter of 200 nm. Although the yield stress obtained for the 20 nm-thickness film and the 200 nm-one has a slight deviation, they approximately follow the Hall-Petch relation.

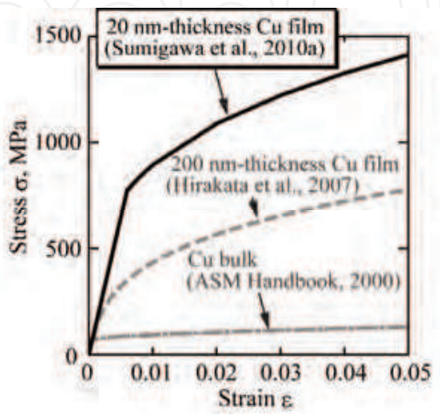

Fig. 9. Dependence of stress-strain relationship on film thickness. The solid line shows Eq. (3).

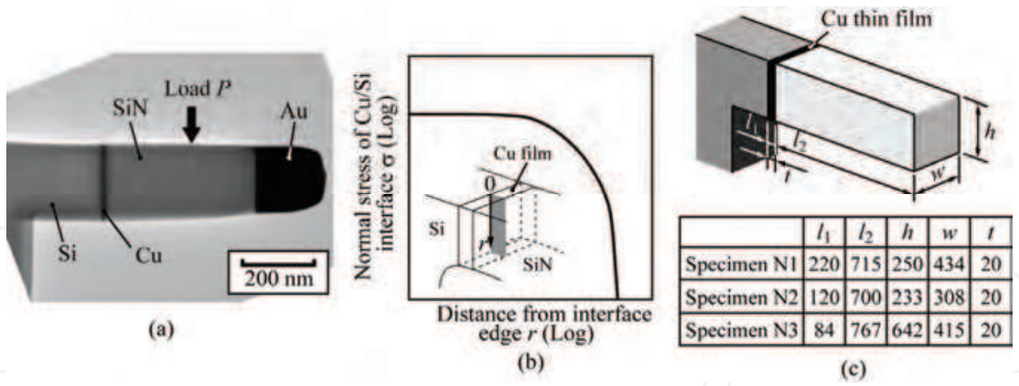

	l_1	l_2	h	w	t
Specimen N1	220	715	250	434	20
Specimen N2	120	700	233	308	20
Specimen N3	84	767	642	415	20

(c)

Fig. 10. (a) TEM image of a specimen (Specimen N1), (b) schematic illustration of stress distribution along the Si/Cu interface, and (c) dimensions of specimens.

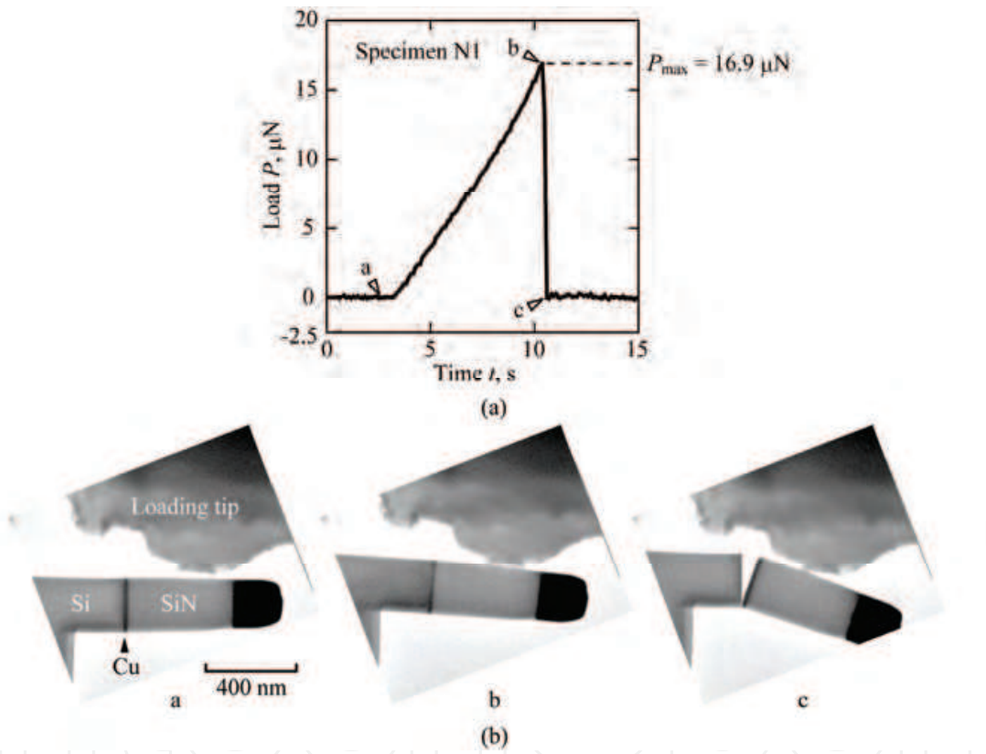

Fig. 11. (a) Load-time relationship, and (b) *in-situ* observation of the interfacial fracture of Specimen N1.

3.2 Crack initiation at the interface edge between Si substrate and 20 nm-thickness Cu film (Sumigawa et al., 2010b)

3.2.1 Research target and experimental detail

At a dissimilar interface edge, stress is concentrated owing to the free-edge effect (Bogy, 1968). Although an interfacial crack may appear at the top interface edge in the cantilever specimen, the cracking criterion on the basis of continuum mechanics such as "critical stress" is questionable in a nano-component because only a few tens or a few hundreds

atoms exist in the stress concentrated region. The target in this section is to examine the dominant factor of crack initiation at the dissimilar interface edge in nano-components by using the bending experiment under the *in-situ* TEM observation.

Figure 10(a) shows a TEM image of specimen for interfacial cracking experiment. Because the strength of interface between Si and Cu is weaker than that between Cu and SiN, the Si/Cu interface is broken preferentially.

Figure 10(b) schematically illustrates the stress distribution along the Si/Cu interface in the specimen. A crack is initiated at the interface edge on the top surface. Three specimens (Specimen N1, N2, and N3) with different size are prepared in order to change the stress distribution along the Si/Cu interface. The size of specimens is summarized in Fig. 10(c).

3.2.2 Criterion of crack initiation

Figure 11 (a) shows the loading curve (*P*-*t* relationship) of Specimen N1. The load, *P*, monotonically increases up to a peak magnitude of 16.9 μN (point b) and then abruptly drops to 0 μN (point c). Figure 11(b) shows bright-field TEM images corresponding to the points a, b and c on the *P*-*t* curve. The crack is initiated at the point b at the top interface edge and instantly propagates along the interface. Detailed observation after the experiment demonstrates that no dissimilar material remained on either delaminated surfaces, confirming pure interface-cracking. Similar behaviour is observed in Specimens N2 and N3. Thus, the peak loads for interfacial crack initiation, P_c, are critical, and Table 2 lists the magnitudes of P_c. There are significant differences in P_c among the specimens.

The stress in the specimen is analyzed by the FEM, in which an individual model is prepared for each experimental specimen. Figure 12(a) shows the analytical model of Specimen N1, where the configuration is reconstructed on the basis of the SEM and TEM micrographs. The constitutive equation obtained in previous section (Eq. (3)) is used for Cu film.

	P_c (μN)
Specimen N1	16.9
Specimen N2	10.3
Specimen N3	85.3
Specimen S1	57.9

Table 2. Critical load for crack initiation at Si/Cu interface.

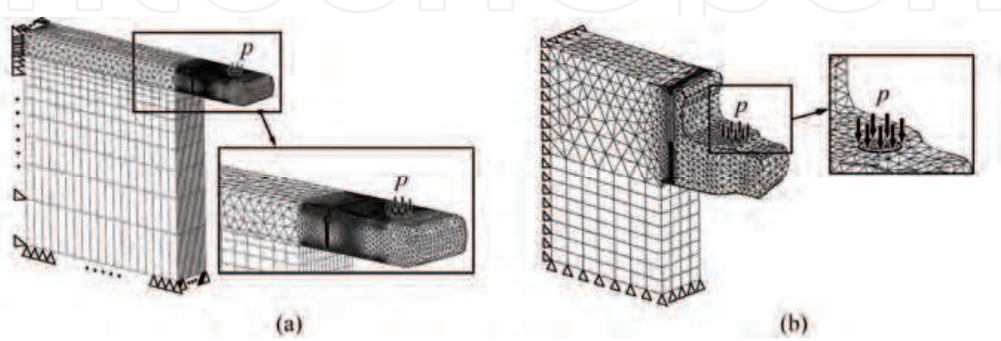

Fig. 12. Mesh division in FEM analysis: (a) Specimen N1 and (b) Specimen S1.

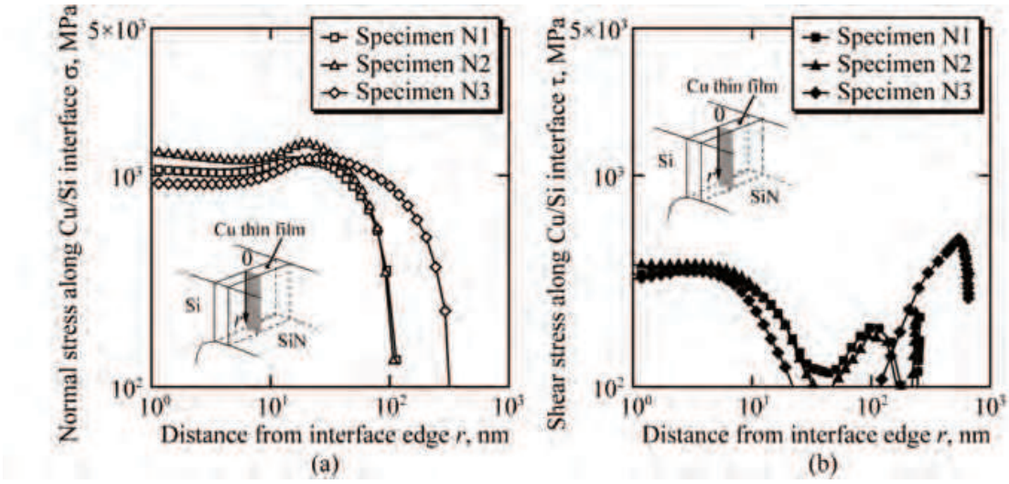

Fig. 13. Elasto-plastic stress distributions along Si/Cu interface near the edge: (a) normal stress σ and (b) shear stress τ.

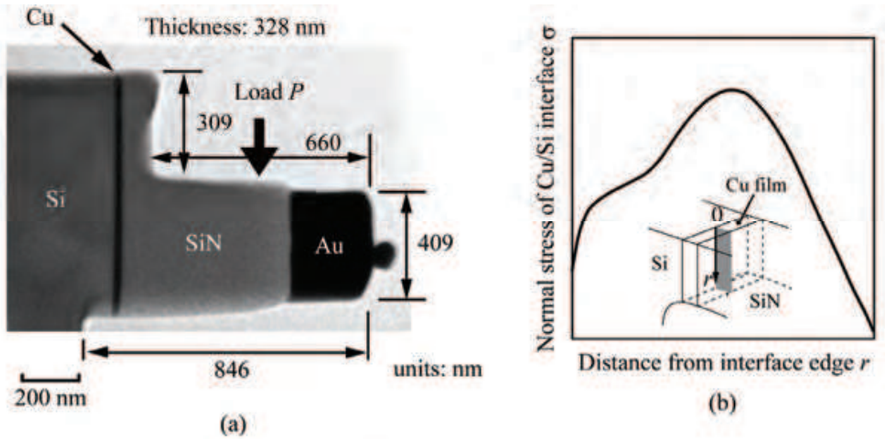

Fig. 14. (a) TEM image and dimensions of Specimen S1, and (b) stress distribution along the Si/Cu interface.

Figure 13 shows the distribution of normal and shear stresses, σ and τ, along the Si/Cu interface near the edge at the critical load P_c. Although the stresses away from the edge in Specimens N1 to N4 differ from each other, they show fairly good agreement in the range of 20-30 nm near the edge. This indicates that crack initiation is governed by the concentrated stress. The high normal stress of about 1 GPa in a region of a few tens of nanometers near the interface edge, which is approximately three-times larger than that of the shear stress ($\tau \approx 300$ MPa), governs the crack initiation.

3.3 Crack initiation in the interior of the interface between Si substrate and 20 nm-thickness Cu film (Sumigawa et al., 2010b)

3.3.1 Research target and experimental detail

Stress concentration does not always take place at the interface edge because of the complex shapes of nano-components. Because the edge has a peculiar atomic arrangement, the

fracture resistance is expected to be different from the one of interface inside of the component. This suggests that interface crack initiation is dependent upon the location in the component. In this section, an experiment where a crack is initiated in the interior of the dissimilar interface is conducted, and the difference in the crack initiation criteria along the interface at the edge and in the interior is discussed.

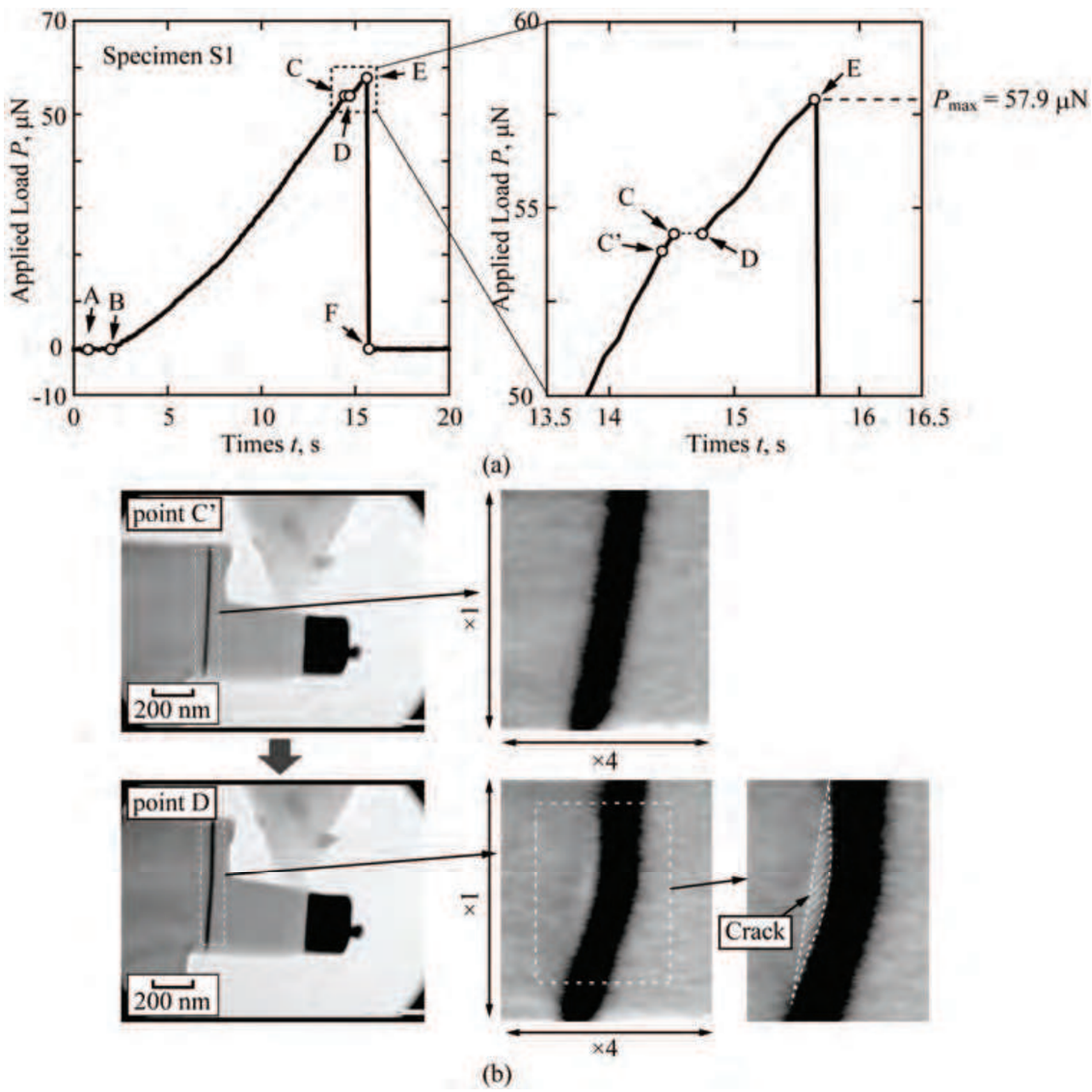

Fig. 15. (a) Load-time relationship of Specimen S1 and (b) detailed TEM images before and after the crack initiation.

Figure 14(a) shows a TEM image of specimen with a step in the SiN portion of cantilever. Figure 14(b) schematically illustrates the stress distribution along Si/Cu interface in the specimen. While there is no stress concentration at the interface edge, the stress has the maximum in the central region of the Si/Cu interface. This suggests that an interfacial crack is initiated in the interior of the Si/Cu interface.

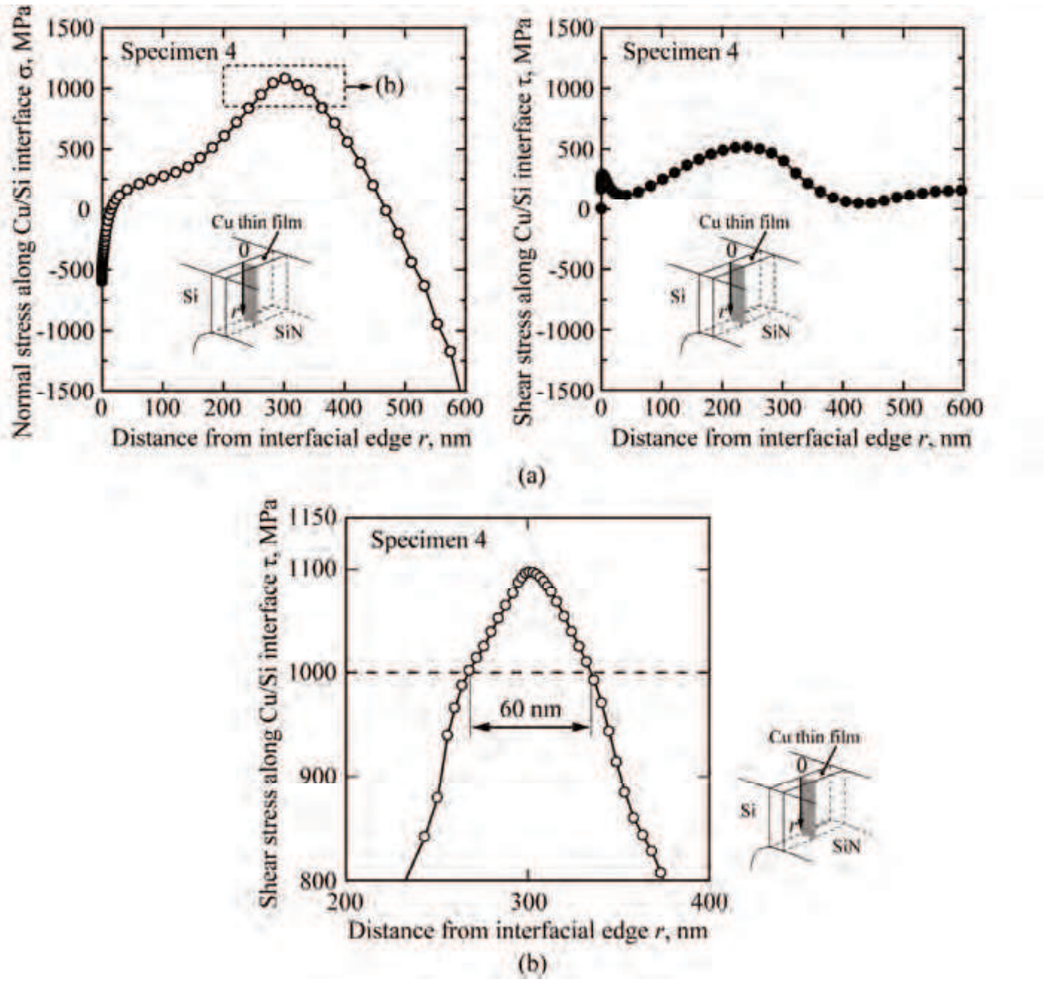

Fig. 16. Stress distributions along the Si/Cu interface (Specimen S1).

3.3.2 Criterion of crack initiation

Figure 15(a) shows the *P*-*t* relationship for Specimen S1. *P* monotonically increases up to *P* = 54.3 μN (point C), and it jumps from C to D. Then, the load begins to increases again before the sharp drop at the point E. Figure 15(b) shows sequential TEM micrographs corresponding to the points on the *P*-*t* curve. The interface is suddenly bent at the jump C-D, and a crack shown in the lower photo in Fig. 15 (b) appears at the location of r = 300 nm from the interface edge on the upper surface. Finally, the crack instantaneously propagates along the interface at point E (P = 57.9 μN).

Figure 16(a) shows the distributions of normal stress, σ, and shear stress, τ, at P = 54.3 μN along the Si/Cu interface, which are obtained by using an FEM model shown in Fig. 12(b). σ has a peak concentration at $r \approx 300$ nm, which corresponds to the experimentally observed portion of crack initiation. Because σ at $r \approx 300$ nm is much larger than that of τ, the former is the dominant factor in the crack initiation. Figure 16(b) shows a magnified view of the σ-distribution near r = 300 nm. The maximum stress is about 1.1 GPa, and the region of $\sigma > 1$ GPa extends about 60 nm.

Comparing the results shown in Figs. 13(a) and 16(b), crack initiation in the interior has the following characteristics:

1. The critical stresses in both cases are of almost the same magnitude, about 1 GPa.
2. The high-stress regions in both cases are several tens of nanometers in width, but the interior crack initiation requires a slightly wider region.

In short, there is little difference between the crack initiation criteria along the interface at the edge and in the interior.

3.4 Fatigue cracking (Sumigawa et al., 2010c)

3.4.1 Research target and experimental detail

Since typical fatigue substructures in a bulk metal, of which size is in the scale of a few micrometers (Mughrabi, 1978), cannot form in a nano-component. However, the fatigue of nano-component has not been clarified yet because of the experimental difficulty. The target in this section is to examine the fatigue behaviour of metal in a nano-component using the bending cantilever under the *in-situ* TEM observation.

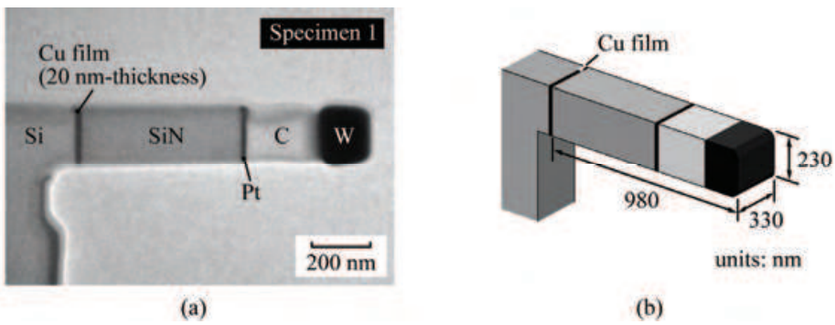

Fig. 17. (a) Bright-field TEM image of specimen, and (b) dimensions of specimens.

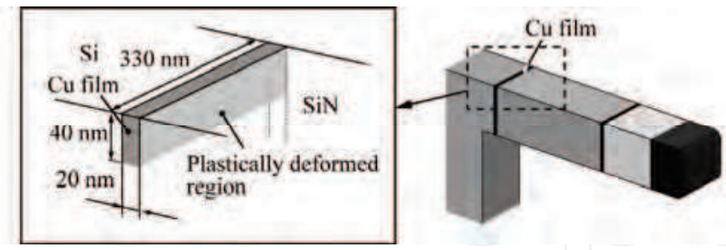

Fig. 18. Fatigue region (plastically deformed region) in the Cu film.

Figure 17 shows (a) a bright-field TEM image of specimen and (b) its size. It should be noted that the stress concentration near the Si/Cu interface obtained by the FEM analysis points out the fatigue region is about 40 nm×20 nm×330 nm in the Cu film as schematically illustrated in Fig. 18.

The fatigue experiment is conducted under a constant load range, $\Delta P = P_{max}$-P_{min}, with a load ratio of $P_{min}/P_{max} = 0$ (P_{min}: minimum load, P_{max}: maximum load). The initial load range is 8 μN, which is increased to 9 μN after 100 cycles. This process of fatigue (100 cycle) and load increase (1 or 1.5 μN) is repeated until the specimen breaks under $\Delta P = 18$ μN (See Fig. 19).

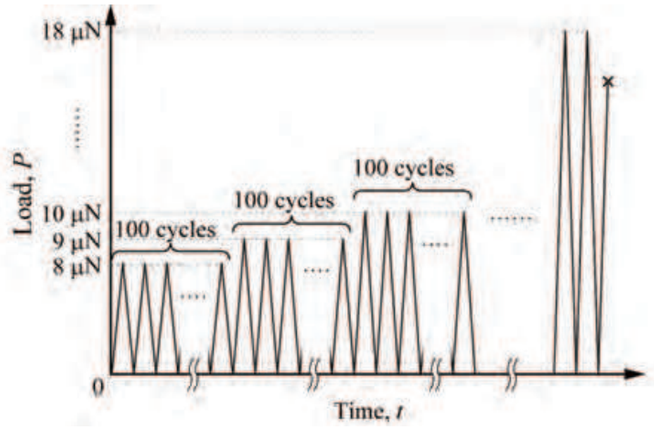

Fig. 19. Schematic illustration of the loading condition of fatigue experiment with a constant load range.

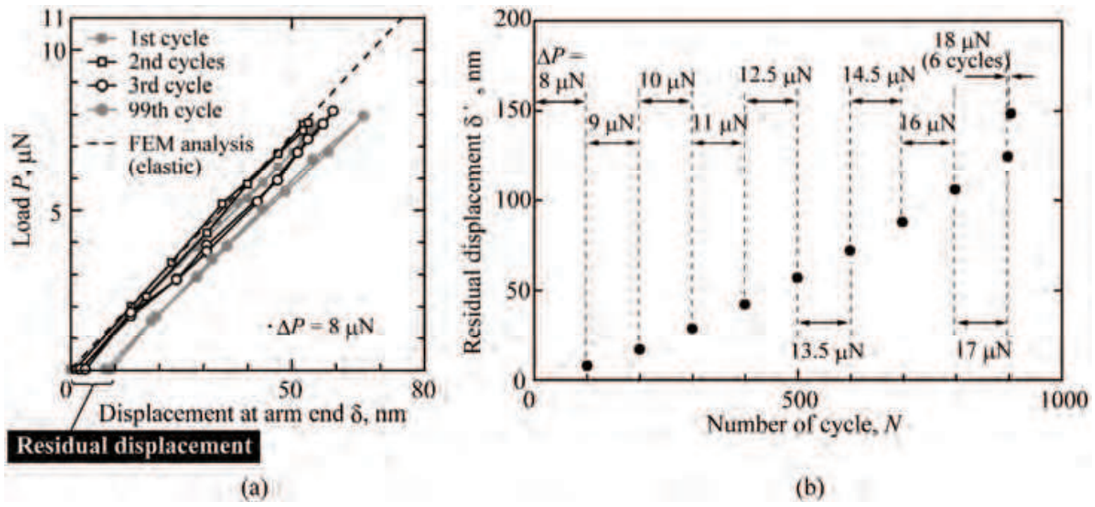

Fig. 20. (a) Load-displacement curves at 1st, 2nd, 3rd, and 99th cycles under the initial load range (ΔP = 8 μN), and (b) residual displacement, δ', with respect to the number of cycles, N.

3.4.2 Fatigue of 20 nm-thick Cu and cracking along Si/Cu interface

Figure 20(a) shows the load-displacement (P-δ) curves in the 1st, 2nd, 3rd, and 99th cycles under the initial load range (ΔP = 8 μN). In the figure, the broken line shows the relation obtained from elastic FEM analysis. The linear and reversible behaviour in each cycle indicates that the specimen, including the Cu layer, elastically deforms under the cyclic loading. The fact that the P-δ curves experimentally obtained are in a good agreement with the analytical one indicates the sufficient accuracy in the control/measurement of load and displacement. The gradient of the P-δ curve does not change until the last cycle. The elastic deformation ensures the reliability of our system in fatigue, where long-term stability of the experimental system is essential.

Careful examination of the P-δ relation reveals that irreversible residual displacement, δ', of about 10 nm is accumulated until the last cycle. Considering the measurement precision, this

signifies the accumulation of plastic strain in the specimen though the magnitude in each cycle cannot be individually identified. Figure 20(b) shows δ' in the last cycle under each load range revealing that irreversible (plastic) strain accumulates with the progress of cyclic deformation. In particular, δ' rapidly increases under ΔP = 18 μN.

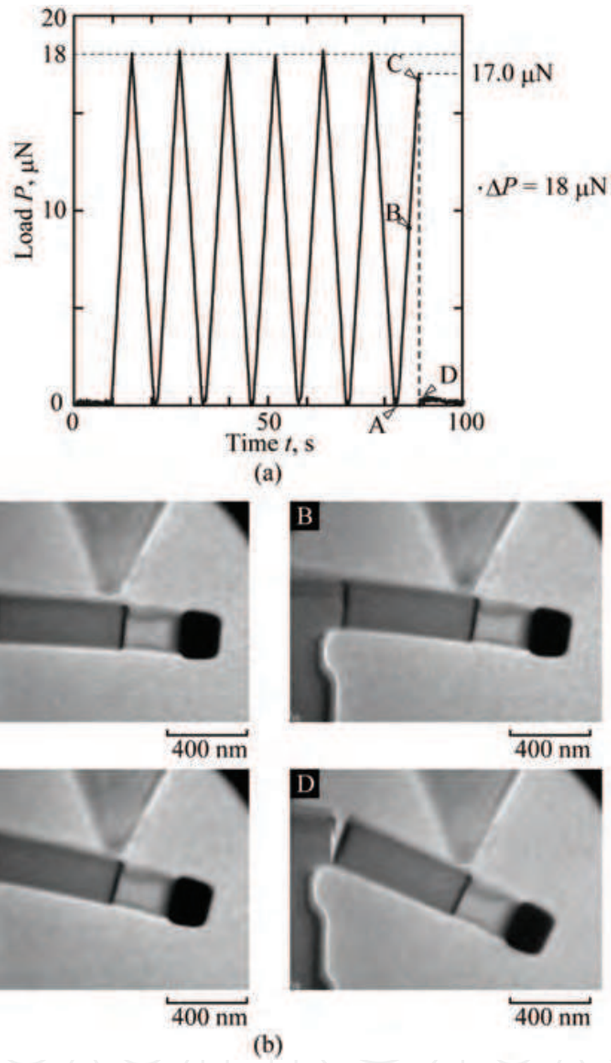

Fig. 21. (a) Load-time relationship under the load range of 18 μN, and (b) TEM micrographs in the 7th cycle.

The specimen breaks in the 7th cycle under ΔP = 18 μN. Figure 21 shows (a) the load-time (P-t) relationship under ΔP = 18 μN and (b) bright-field TEM images corresponding to the alphabets in the P-t relationship. The specimen is cyclically loaded until the 6th cycle without any damage observed on the interface. In the 7th cycle, the load suddenly drops before the maximum load (17.0 μN; point C in Fig. 21(a)), and the specimen breaks along the Si/Cu interface. Since the load at C is about 6 % smaller than P_{max} = 18 μN, it is clearly different from the fracture in a monotonic loading. The TEM images in Fig. 21(b) show that there is no remarkable damage in the Si/Cu interface before the break.

Figure 22 shows the *P-δ* curves in each cycle. The nonlinear behaviour and distinct hysteresis loop indicate the cyclic plasticity of the Cu film because the Si substrate and the SiN layer elastically deforms at this load level. After the 2nd cycle, reverse yielding appears during the unloading process. These suggest the development of a cyclic substructure in the Cu film.

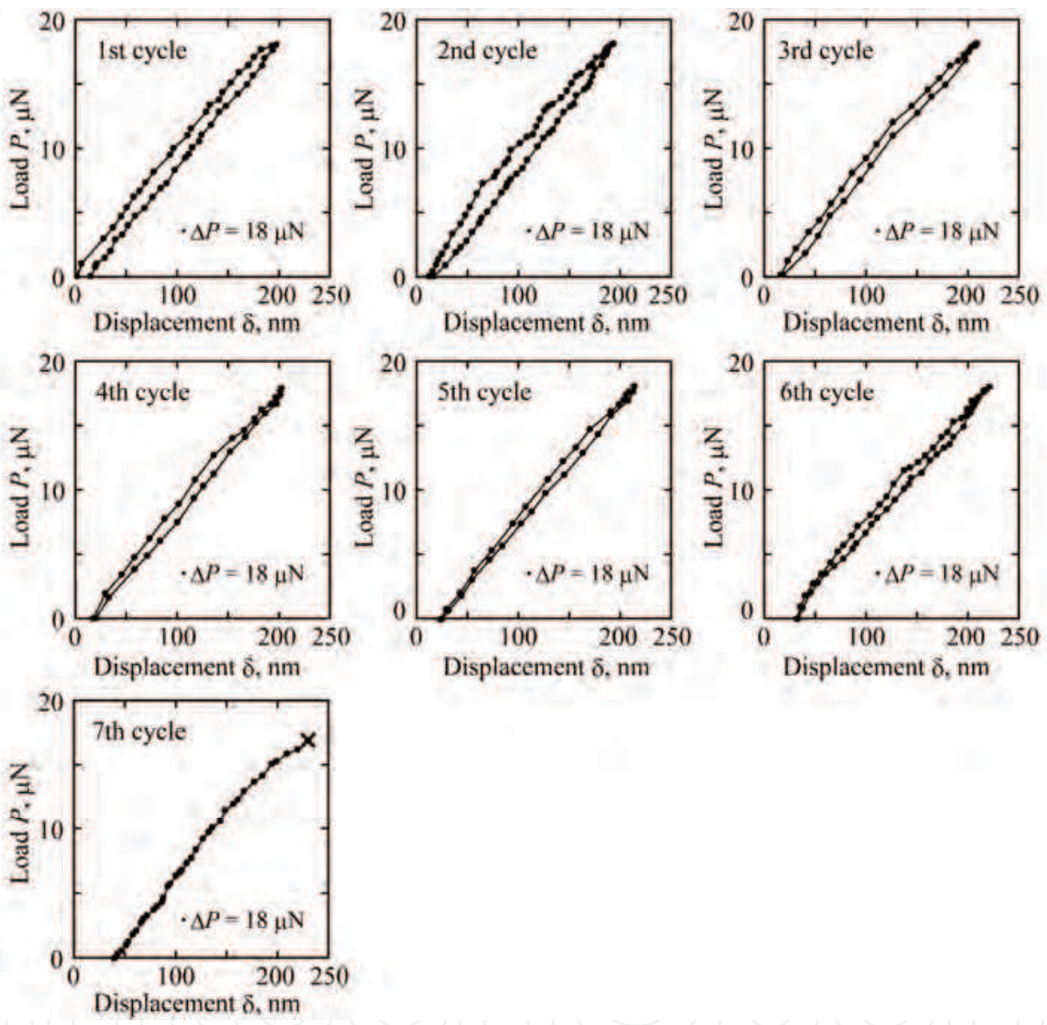

Fig. 22. Load-displacement curves under the load range of 18 μN.

As shown in Fig. 20(b), the residual displacement increases rapidly after the load range is increased to ΔP = 18 μN. The average in one cycle is 4.0 nm, which is more than one-order larger than that under ΔP = 17 μN. This drastic softening of the Cu film may also be due to the transition and development of the cyclic substructure. The width of the cyclic *P-δ* curve becomes narrower with increasing number of fatigue cycles. Figure 23 shows the half bandwidth of the cyclic loop, $w_{1/2}$, with respect to the number of cycles. $w_{1/2}$ gradually decreases with the progress of cyclic deformation, and the magnitude in the 6th cycle is about half of that in the 1st cycle. This indicates cyclic hardening in the Cu film due to the transition of the substructure.

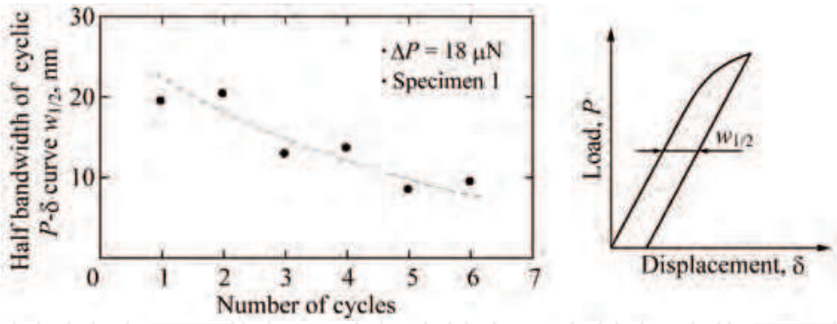

Fig. 23. Change of half bandwidth of the *P-δ* loop under the load range of 18 μN.

3.5 *In-situ* transmission observation of plasticity in 200 nm-thickness Cu film near Si/Cu interface edge (Sumigawa et al., 2011a)

3.5.1 Research target

High-voltage TEM observation enables us to investigate the understructure at the nano- or atomic scale in materials. However, it is not convenient to handle and requires heavy economic load to the researches. If we can conduct the *in-situ* observation by a general-purpose TEM, it is great help for the researcher to seek the understanding of precise mechanism in a nano-scale component. For the sake of *in-situ* observation by a general-purpose TEM, the testing section must be thinned to about 100 nm. In order to observe the understructure of the specimen, a trial is discussed in this section.

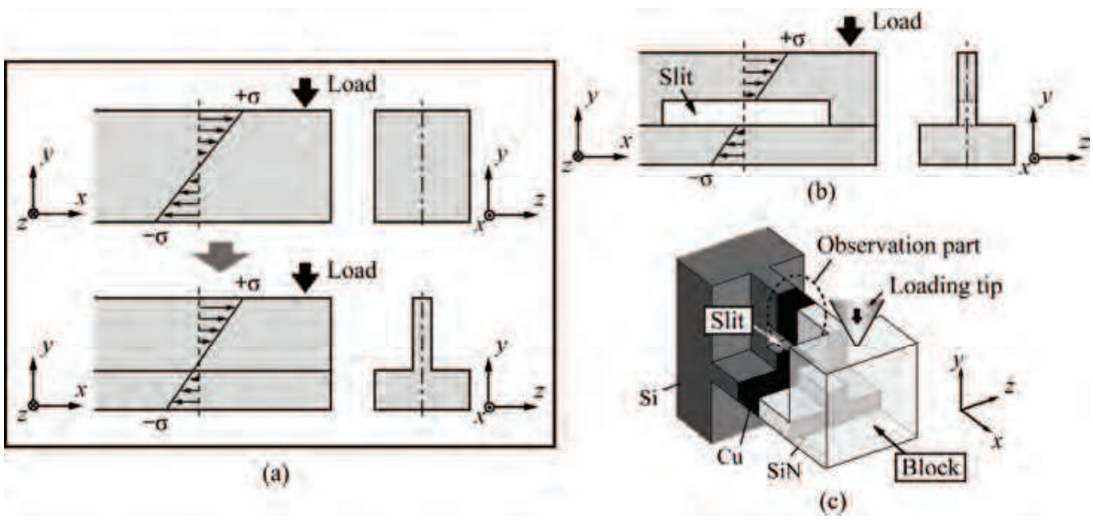

Fig. 24. (a) Cantilever specimen with the cross section of inverted-T-shape, (b) introduction of a horizontal through slit, and (c) final concept of specimen configuration and loading experiment.

3.5.2 Specimen and fabrication procedure

In bending test, the specimen buckles at the thin part under the compressive stress. In order to prevent the buckling at the lower part, the specimen with an inverted-T-shaped cross-section, where the neutral plane of bending deformation locates near the bottom, is adopted

in order to confine the compressive stress to the thicker portion (Fig. 24(a)). Moreover, by introducing a horizontal through-slit in the center of the thinned part, we can surely apply tensile stress in the experimental area (Fig. 24(b); thin part). A block with high rigidity is added at the end of the cantilever for loading by a diamond tip. The final concept of the specimen configuration is schematically illustrated in Fig. 24(c).

The specimen is fabricated by means of a FIB processing. The fabrication procedure is described in detail below.

1. Gold (Au) with a thickness of 500 nm is deposited on the multi-layered plate (Si substrate/Cu (200 nm thickness)/SiN (500 nm thickness)) to protect the SiN layer from the ion beam.
2. A 10 μm×10 μm×10 μm block is carved out from the multi-layered plate, and is mounted on the flat top of an Au wire (wire diameter: 250 μm, and diameter of flat top: 100 μm) with an adhesive (Figs. 25(a)-(c)) so that the dissimilar interfaces (Si/Cu and Cu/SiN interfaces) are vertically aligned on the wire top (Fig. 25(c)).
3. A part of the block is thinned to less than 1500 nm in the thickness by a *z*-direction beam (beam current: 50-1000 pA) (Fig. 25(d)).
4. The thinned part is processed to about 500 nm in the thickness by a weak beam (beam current: 30 pA) (Fig. 25(e)).
5. After the horizontal through-slit is introduced in the specimen by a *y*-direction beam (beam current: 4 pA) (Fig. 25(f)-(i)), the thinned part is processed to less than 100 nm in the thickness by a *z*-direction beam (beam current: 4 pA).
6. The upper surface is finished from the *x*-direction (beam current: 4 pA) (Figs. 25(f)-(ii)), and the bottom is processed from the *y*-direction to complete the cantilever specimen (Fig. 25(f)-(iii)).

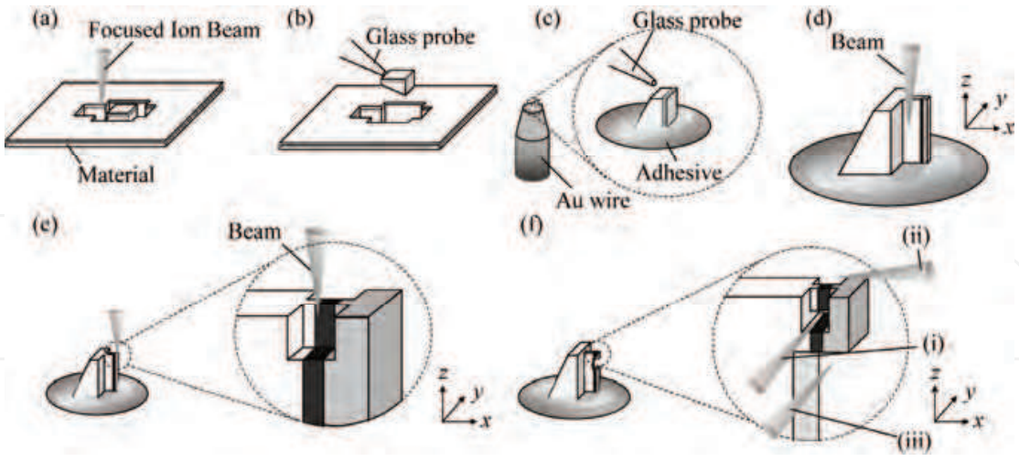

Fig. 25. Schematic illustration of the specimen preparation procedure.

3.5.3 Observation of plastic region

Figure 26(a) shows SEM images of fabricated specimen, in which the thickness of the thinned portion is about 75 nm. The block size at the cantilever end is 550 nm×310 nm×700 nm. Au at the specimen end is a protection layer for FIB processing. Figure 26(b) shows the configuration and size of the specimen without the Au passivation layer.

Figure 27 shows a bright-field TEM image of the specimen. The magnified view in Fig. 27 shows no grain boundary near the Si/Cu interface edge though the Cu film is polycrystalline material. As the average diameter of grins is about 300 nm, the region near the edge is occupied by a single crystal. In general, elastic deformation and lattice distortion due to a dislocation brings about inhomogeneous contrast in a TEM image. Since there is no contrast difference observed near the Si/Cu interface edge in Fig. 27 before loading, the initial dislocation density is almost constant in this region.

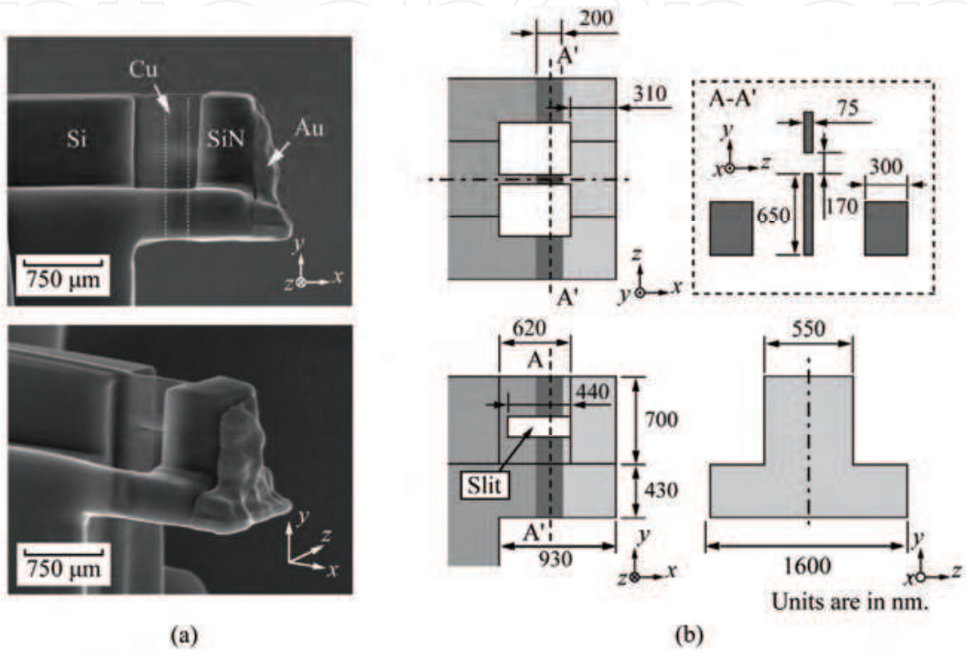

Fig. 26. (a) SEM image, and (b) size of specimen.

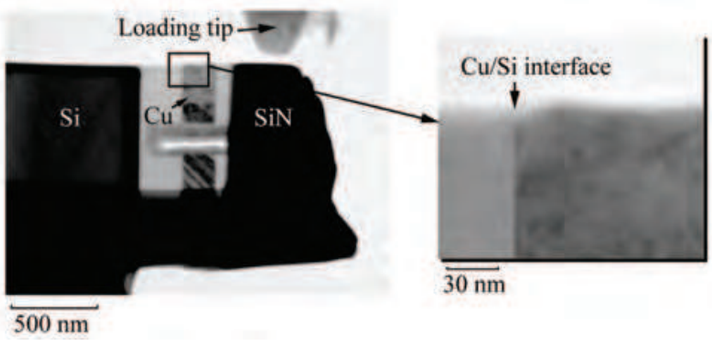

Fig. 27. TEM image of specimen.

Figure 28 shows the specimen model for the FEM analysis, which is precisely reconstructed following the actual specimen shape. Although microscopic structures such as grains would affect the deformation of the Cu and SiN, isotropic homogeneity is assumed because the focus is on an approximate evaluation of the stress distribution here.

Figure 29 shows a distribution of the normal stress σ_x along the Si/Cu interface near the upper edge. The stress is normalized by a reference stress σ' which is σ_x at the center of the

upper surface in the Cu film (indicated by an × in Fig. 28). There is no compressive stress in the test area, and tensile stress prevails as designed. The stress concentrates within about several tens of nm from the interface edge because of the deformation mismatch between the Cu film and the Si substrate.

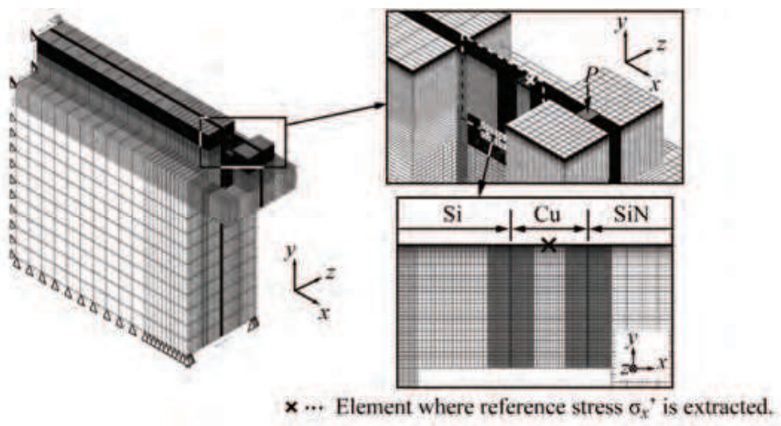

Fig. 28. Model for finite element analysis.

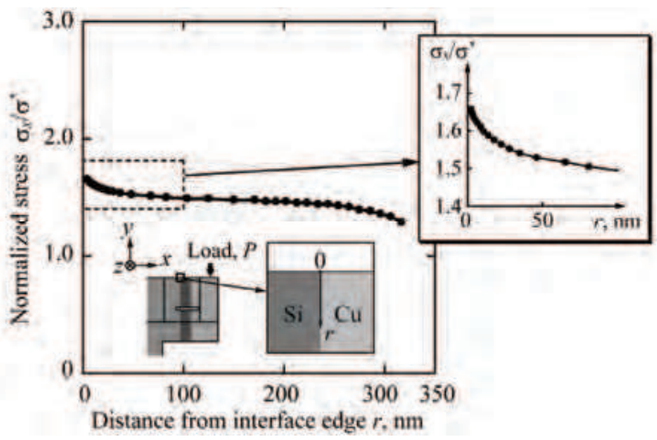

Fig. 29. Distribution of normalized reference stress, σ_x/σ_x', along the Si/Cu interface.

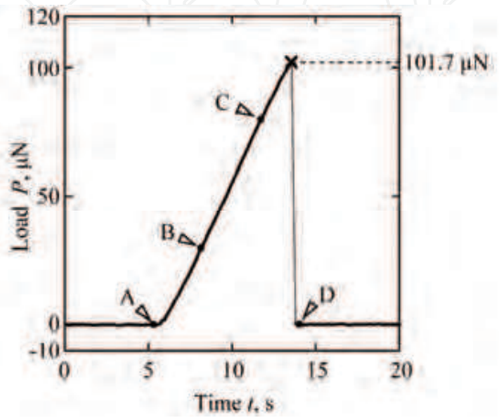

Fig. 30. Load-time relationship.

Figure 30 shows the load-time relationship obtained from the bending experiment. After the load P linearly increases, it suddenly drops at P = 101.7 μN.

Figure 31 shows a series of TEM images during the experiment. These indicate that the loading tip firmly touches the block at the cantilever end without slip at the contact. The specimen breaks along the Si/Cu interface when the load reaches P = 101.7 μN. No buckling takes place in the specimen before breaking.

The dark area indicated by a dashed circle in Fig. 31 (B) appears near the interface edge in the Cu film at about P = 20 μN. The area gradually expands as the load increases (See Fig. (C)). The location corresponds to the stress-concentration region predicted by FEM analysis (See Fig. 29). If the shadow is caused by a local elastic deformation, the boundary of dark area is vague due to the stress distribution. However, the shadow in the images has a clear boundary. These indicate that the area is caused by plastic deformation. The shadowed area expands along the upper surface of the specimen with increasing the applied load. The plastic region near the Si/Cu interface edge is determined by image processing, and Fig. 33 shows the change in the area. A definite plastic region appears at P = 20 μN and reaches about 920 nm^2 at P = 80 μN.

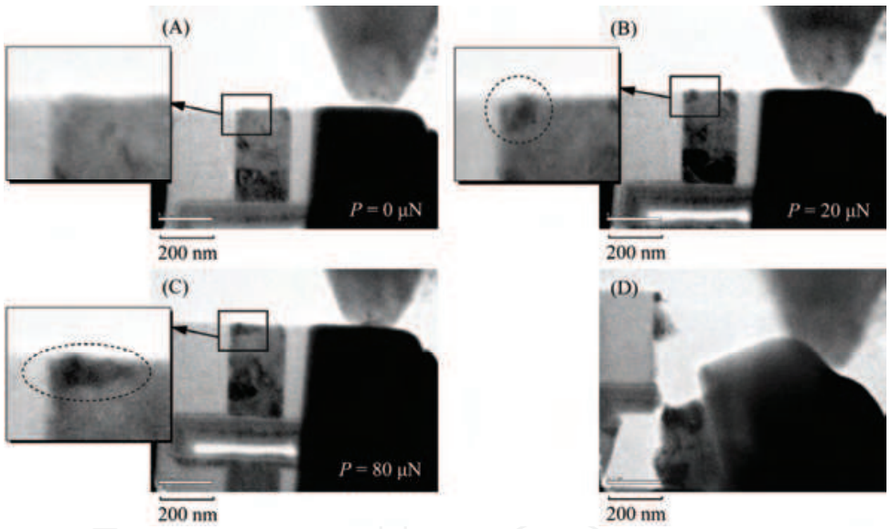

Fig. 31. *In-situ* TEM images during bending deformation.

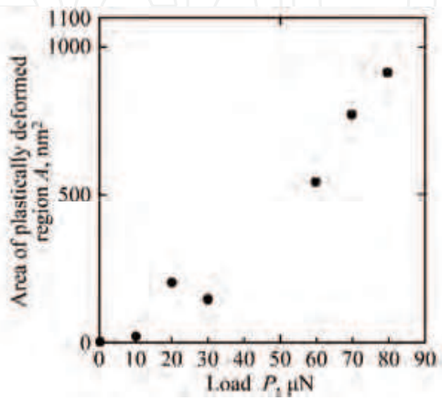

Fig. 32. Change of area where plastic deformation occurs.

4. Conclusion

This chapter highlights bending experiments on the strength of nano-scale interface with *in-situ* TEM observation. Cantilever specimens are carved out of a multi-layered material where a 20 nm-thick Cu film is sandwiched between a SiN layer and a Si substrate by means of the FIB processing. The results are summarized as follows.

- TEM image enables us to quantitatively measure the displacement at the arm end of specimen during the bending experiment.
- The elastic-plastic constitutive equation of the Cu portion can be estimated by an inverse analysis using the load-displacement relationship.
- Crack initiation at Si/Cu interface edge under monotonic loading is governed by the normal stress of about 1 GPa in a region of 20 – 30 nm.
- A Specimen with a step in the SiN portion induces a crack initiation at the interior Si/Cu interface owing to the stress concentration. There is little difference between the crack initiation criteria along the interface at the edge and in the interior.
- Under cyclic loading, the Cu portion evidently shows fatigue behaviour, and then, the specimen breaks along the Si/Cu interface by the fatigue.
- Cantilever specimen with an inverted-T-shaped cross-section, a through-slit in the thinned part, and a rigid block at the arm end is designed for the *in-situ* observation inside of nano-component. It enables us to conduct a bending experiment with *in-situ* transmission observation, which can observe the plastic zone in the Cu portion.

The mechanical properties in nano-components are described in detail in a book "Fracture nanomechanics" (Kitamura et al., 2011).

There are further challenging topics on the mechanical behaviour of nano-component remained. For example, although the Section 3.2 demonstrates that continuum mechanics is still valid in the range of 20-30 nm and the stress concentration can describe fracture characteristics, the applicability in smaller regions is unclear. Moreover, the mechanism of plasticity and the cyclic substructure in nano-component are not clarified. Since the ratio of the surface to the volume in nano-components is remarkably large, the mechanical properties are strongly affected by corrosion and surface diffusion. Consequently, the deformation and fracture behaviour under an environment and a high-temperature is of great interest. The technique described in this chapter may greatly contribute to future research on the mechanical property of nano-components.

5. Acknowledgment

We acknowledge financial support by a Grant-in-Aid for Scientific Research (S)(No.21226005), from the Japan Society for the Promotion of Science, and by a Grant-in-Aid for Young Scientists (A)(No. 21686013), from the Ministry of Education, Culture, Sports, Science and Technology, Japan.

6. References

ASM Handbook (2000). *Mechanical Testing and Evaluation Vol.8*, ASM International, Metals Park, Ohio, p. 103

Bogy, DB. (1968). Edge-bonded Dissimilar Orthogonal Elastic Wedges under Normal and Shear Loading. *Journal of Applied Mechanics*, Vol.35, pp. 460-466

Burdess, J.S.; Harris, A.J.; Wood, D.; Pitcher, R.J. & Glennie, D. (1997). A System for the Dynamic Characterization of Microstructures. *Journal of Microelectromechanical Systems*, Vol.6, pp. 322–328

Cheng, Y.-W.; Read, D.T.; McColskey, J.D,; Wright, J.E. (2005). A Tensile-testing Technique for Micrometer-sized Free-standing Thin Films. *Thin Solid Films*, Vol.484, pp. 426-432

Dao,M.; Chollacoop, N.; Vliet, K.J.V.; Venkatesh, T.A. & Suresh, S. (2001). Computational Modeling of the Forward and Reverse Problems in Instrumented Sharp Indentation. *Acta materialia*, Vol.49, pp. 3899–3918

Dimiduk, D.M.; Uchic, M.D. & Parthasarathy, T.A. (2005). Size-affected Single-slip Behavior of Pure Nickel Microcrystals. *Acta materialia*, Vol.53, 4065–4077

Greer, J.R. & Nix, W.D. (2006). Nanoscale Gold Pillars Strengthened through Dislocation Starvation. *Physical Review B*, Vol.73, article number 245410

Haque, M.A. & Saif, M.T.A. (2002). In-situ Tensile Testing of Nano-scale Specimens in SEM and TEM. *Experimental Mechanics*, Vol.42, No.1, pp. 123-128

Hou, C.; Li, Z.; Huang, M. & Ouyang, C. (2008). Discrete Dislocation Plasticity Analysis of Single Crystalline Thin Beam under Combined Cyclic Tension and Bending. *Acta Materialia*, Vol.56, pp. 1435–1446

Hua, T.; Xie, H.; Pan, B.; Qing, X.; Dai, F. & Feng, X. (2007). A New Micro-tensile System for Measuring the Mechanical Properties of Low-dimensional Materials — Fibers and Films. *Polymer Testing*, Vol.26, pp. 513–518

Huang, H. & Spaepen, F. (2000). Tensile Testing of Free-standing Cu, Ag and Al Thin Films and Ag/Cu Multilayers. *Acta Materialia*, Vol.48, pp. 3261-3269

Huang, Y.; Xue, Z.; Gao, H.; Nix, W.D. & Xia, Z.C. (2000). A Study of Microindentation Hardness Tests by Mechanism-based Strain Gradient Plasticity. *Journal of Material Research*, Vol.15, No.8, pp. 1786-1796

Hirakata, H.; Takahasi, Y. ; Truong, D.V. & Kitamura, T. (2007). Role of Plasticity on Interface Crack Initiation from a Free Edge and Propagation in a Nano-component. *International Journal of Fracture*, Vol.145, No.4, pp. 261-271

Keller, R.R.; Phelps, J.M. & Read, D.T. (1996). Tensile and Fracture Behavior of Free-standing Copper Films. *Materials Science and Engineering A*, Vol.214, pp. 42-52

Kim, J.S. & Huh, H. (2011). Evaluation of the Material Properties of an OFHC Copper Film at High Strain Rates Using a Micro-Testing Machine. *Experimental Mechanics*, Vol.51, pp. 845–855

Kitamura, T.; Hirakata, H.; Sumigawa, T. & Shimada, T. (2011). *Fracture Nanomechanics*, Pan Stanford Publishing Pte. Ltd., Singapore

Komai, K.; Minoshima, K. & Inoue, S. (1998). Fracture and Fatigue Behavior of Single Crystal Silicon Microelements and Nanoscopic AFM Damage Evaluation. *Microsystem Technologies 5*, pp. 30-37

Li, X.; Kasai, T.; Nakao, S.; Tanaka, H.; Ando, T.; Shikida, M. & Sato, K. (2005). Measurement for Fracture Toughness of Single Crystal Silicon Film with Tensile Test. *Sensors and Actuators A*, Vol.119, pp. 229–235

Liu, Z.L.; Liu, X.M.; Zhuang, Z. & You, X.C. (2009). A Multi-scale Computational Model of Crystal Plasticity at Submicron-to-nanometer Scales. *International Journal of Plasticity*, Vol. 25, pp. 1436–1455

Namazu, T.; Isono, Y. & Tanaka, T. (2000). Evaluation of Size Effect on Mechanical Properties of Single Crystal Silicon by Nanoscale Bending Test using AFM. *Journal of Microelectromechanical Systems*, Vol.9, No.4, pp. 450-459

Namazu, T.; Isono, T. & Tanaka, T. (2002). Plastic Deformation of Nanometric Single Crystal Silicon Wire in AFM Bending Test at Intermediate Temperatures. *Journal of Microelectromechanical Systems*, Vol.11, No.2, pp. 125-135

Moser, B. & Wasmer, K. (2007). Strength and Fracture of Si Micropillars: A New Scanning Electron Microscopy-based Micro-compression Test. *Journal of Material Research*, Vol.22, No.4, pp. 1004-1011

Motz, C.; Schoberl, T. & Pippan, R. (2005). Mechanical Properties of Micro-sized Copper Bending Beams Machined by the Focused Ion Beam Technique. *Acta Materialia*, Vol.53, pp. 4269–4279

Mughrabi, H. (1978). The Cyclic Hardening and Saturation Behaviour of Copper Single Crystals. *Materials Science and Engineering*, Vol.33, pp.207-223

Ruud J.A.; Josell, D. & Spaepen, F. (1993). A New Method for Tensile Testing of Thin Films, *Journal of Materials Research*, Vol.8, pp. 112-117

Ryu, J.; Kim, J.-H.; Chu, S.; Lee, S. & Moon, S. (2006). Fabrication and Mechanical Characterization of Micro Electro Mechanical System based Vertical Probe Tips for Micro Pad Measurements. *Japanese Journal of Applied Physics*, Vol.45, No.12, pp. 9238–9243

Sumigawa, T.; Shishido, T.; Murakami, T,; Iwasaki, T. & Kitamura, T. (2010a). Evaluation on Plastic Deformation Property of Copper Nano-film by Nano-scale Cantilever Specimen. *Thin Solid Films*, Vol.518, pp. 6040–6047

Sumigawa, T.; Shishido, T.; Murakami, T. & Kitamura, T. (2010b). Interface Crack Initiation due to Nano-scale Stress Concentration. *Materials Science and Engineering A*, Vol.527, pp. 4796–4803

Sumigawa, T.; Murakami, T.; Shishido, T. & Kitamura, T. (2010c). Cu/Si Interface Fracture due to Fatigue of Copper Film in Nanometer Scale. *Materials Science and Engineering A*, Vol.527, pp. 6518–6523

Sumigawa, T.; Kitagawa, Y. & Kitamura, T. (2011a). Development of In-situ TEM Observation Method on Plasticity in Nanoscale Component. *Journal of Solid Mechanics and Materials Engineering*, Vol.5, No.3, pp. 128-137

Sumigawa, T.; Kitamura, T. & Murakami, T. (2011b). Fatigue Strength of the Cu/Si Interface in Nano-components. *Materials Science and Engineering A*, Vol.528, pp. 5158–5163

Suresh, S. (1998). *Fatigue of Materials - Second Edition*, Cambridge University Press, Cambridge, England

Thompson, N.; Wassworth, N. & Louat, N. (1956). The Origin of Fatigue Fracture in Copper. *Phlosophical Magazine*, Vol.1, No.2, pp. 113-126

Tripathy, S.; Lin, V.K.X; Vicknesh, S. & Chua, S.J. (2007). Micro-Raman Probing of Residual Stress in Freestanding GaN-based Micromechanical Structures Fabricated by a Dry Release Technique. *Journal of Applied Physics*, Vol.101, article numver 063525

Tsuchiya, T.; Tabata, O.; Sakata, J. & Taga, T. (1998). Specimen Size Effect on Tensile Strength of Surface-Micromachined Polycrystalline Silicon Thin Films. *Journal of Microelectromechanical Systems*, Vol.7, No.1, pp. 106-113

Tsuchiya, T.; Inoue, A. & Sakata, J. (2000). Tensile Testing of Insulating Tthin Films; Humidity Effect on Tensile Strength of SiO Films. *Sensors and Actuators*, Vol.82, pp. 286–290

Vinci, R.P.; Zienlinski, E.M. & Bravaman, J.C. (1995). Thermal Strain and Stress in Copper Thin Films. *Thin Solid Films*, Vol.262, pp. 142-153

Weertman, J. & Weertman, J.R. (1964). *Elementary Dislocation Theory*. The Macmillan Company, New York, Collier-Macmillan Limited, London

Winter, A.T. (1978). Nucleation of Persistent Slip Bands in Cyclically Deformed Copper Crystals. *Philosophical Magazine A*, Vol.37, No.4, pp. 457-463

Xiang, Y., Tsui, T.Y. & Vlassak, J.J. (2006). The Mechanical Properties of Freestanding Electroplated Cu Thin Films. *Journal of Material Research*, Vol.21, No.6, pp.1607-1618

Yi, T.; Li, L. & Kim, C.-J. (2000). Microscale Material Testing of Single Crystalline Silicon: Process Efects on Surface Morphology and Tensile Strength. *Sensors and Actuators*, Vol.83, pp. 172–178

Zhu, Y.; Moldovan, N. & Espinosa, H.D. (2005). A microelectromechanical load sensor for *in situ* electron and x-ray microscopy tensile testing of nanostructures. *Applied Physics Letters*, Vol.86, article number 013506

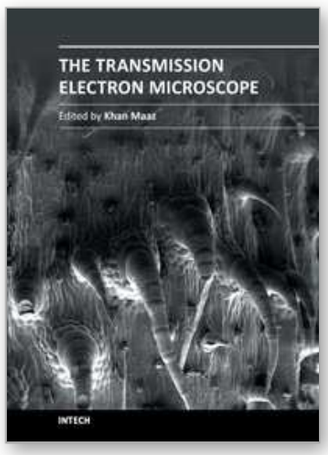

The Transmission Electron Microscope

Edited by Dr. Khan Maaz

ISBN 978-953-51-0450-6
Hard cover, 392 pages
Publisher InTech
Published online 04, April, 2012
Published in print edition April, 2012

The book "The Transmission Electron Microscope" contains a collection of research articles submitted by engineers and scientists to present an overview of different aspects of TEM from the basic mechanisms and diagnosis to the latest advancements in the field. The book presents descriptions of electron microscopy, models for improved sample sizing and handling, new methods of image projection, and experimental methodologies for nanomaterials studies. The selection of chapters focuses on transmission electron microscopy used in material characterization, with special emphasis on both the theoretical and experimental aspect of modern electron microscopy techniques. I believe that a broad range of readers, such as students, scientists and engineers will benefit from this book.

INTECH
open science | open minds

InTech Europe
University Campus STeP Ri
Slavka Krautzeka 83/A
51000 Rijeka, Croatia
Phone: +385 (51) 770 447
Fax: +385 (51) 686 166
www.intechopen.com

InTech China
Unit 405, Office Block, Hotel Equatorial Shanghai
No.65, Yan An Road (West), Shanghai, 200040, China
中国上海市延安西路65号上海国际贵都大饭店办公楼405单元
Phone: +86-21-62489820
Fax: +86-21-62489821

IntechOpen